International Journal of Heat and Fluid Flow 53 (2015) 29–43

Contents lists available at ScienceDirect

International Journal of Heat and Fluid Flow

journal homepage: www.elsevier.com/locate/ijhff

DNS and LES of turbulent flow in a closed channel featuring a pattern of hemispherical roughness elements

D. Chatzikyriakou [a], J. Buongiorno [a,*], D. Caviezel [b], D. Lakehal [a,b]

[a] Massachusetts Institute of Technology, 77 Massachusetts Avenue, Cambridge, MA 02139, USA
[b] ASCOMP GmbH, Zurich, Switzerland

ARTICLE INFO

Article history:
Received 28 August 2014
Received in revised form 6 January 2015
Accepted 9 January 2015

Keywords:
Roughness elements
Turbulent flow
LES
DNS

ABSTRACT

Direct Numerical Simulations (DNS) and Large Eddy Simulations (LES) were performed for fully-developed turbulent flow in channels with smooth walls and walls featuring hemispherical roughness elements at shear Reynolds numbers $Re_\tau = 180$ and 400, with the goal of studying the effect of these roughness elements on the wall-layer structure and on the friction factor. The LES and DNS approaches were verified first by comparison with existing DNS databases for smooth walls. Then, a parametric study for the hemispherical roughness elements was conducted, including the effects of shear Reynolds number, normalized roughness height ($k^+ = 10$–20) and relative roughness spacing ($s^+/k^+ = 2$–6). The sensitivity study also included the effect of distribution pattern (regular square lattice vs. random pattern) of the roughness elements on the walls. The hemispherical roughness elements generate turbulence, thus increasing the friction factor with respect to the smooth-wall case, and causing a downward shift in the mean velocity profiles. The simulations revealed that the friction factor decreases with increasing Reynolds number and roughness spacing, and increases strongly with increasing roughness height. The effect of random element distribution on friction factor and mean velocities is however weak. In all cases, there is a clear cut between the inner layer near the wall, which is affected by the presence of the roughness elements, and the outer layer, which remains relatively unaffected. The study reveals that the presence of roughness elements of this shape promotes locally the instantaneous flow motion in the lateral direction in the wall layer, causing a transfer of energy from the streamwise Reynolds stress to the lateral component. The study indicates also that the coherent structures developing in the wall layer are rather similar to the smooth case but are lifted up by almost a constant wall-unit shift y^+ (~10–15), which, interestingly, corresponds to the relative roughness $k^+ = 10$.

1. Introduction

The effect of wall roughness on the structure of the wall boundary layer has always been a subject of dedicated research, since the pioneering work of Colebrook (1939), Nikuradse (1950). An abundant literature is available for single-phase, turbulent flow in channels with large roughness elements of various shapes – see for instance the review of experimental work provided in Jimenez (2004); however, there is little to cite as to the effect of small hemispherical roughness elements regularly or randomly distributed on the channel wall; a situation that is relevant to various energy systems such as fossil boilers and nuclear reactors, in which vapor bubbles are attached to the wall in subcooled flow boiling and effectively behave like small (<100 μm), near-hemispherical, roughness elements. The objective of this study is to investigate the effects of small solid hemispherical roughness elements on fully developed turbulent channel flow by using high-fidelity DNS and LES simulations. In particular, the effect of shear Reynolds number, roughness size, spacing and distribution (random vs. regular pattern) for roughness elements is explored here in a systematic way.

The size and distribution of the hemispherical roughness elements studied here are informed by the subcooled flow boiling situation in the hot fuel assembly of a Pressurized Water Reactor (PWR). However, here there is no intent to simulate actual bubbles, only small solid hemispherical roughness elements.

Background and a brief literature review are given in Section 2. The numerical procedure is described in Section 3. The DNS and LES studies for smooth wall channel flow and one representative case with hemispherical roughness elements are presented in Section 4. A parametric LES analysis for hemispherical roughness

* Corresponding author.
E-mail address: jacopo@mit.edu (J. Buongiorno).

http://dx.doi.org/10.1016/j.ijheatfluidflow.2015.01.002
0142-727X/

elements is presented in Section 5. The conclusions and recommendations for future work are discussed in Section 6. The LES quality and solution verification are reported in the Appendix.

2. Background

The introduction of high fidelity simulation approaches and ever more powerful computers has allowed a series of DNS studies of fully developed flow over rough-walled rectangular channels with two dimensional ribs, with detailed PIV data (Krogstad et al., 1992, 2005) for model validation. In most of these studies, the ribs were quite large, reaching up to 20% of the channel half height. The effect of rib spacing was studied widely with DNS and LES (Leonardi and Castro, 2010; Miyake et al., 2001; Leonardi and et al., 2003; Nagano et al., 2004; Ashrafian et al., 2004; Hanjalic and Launder, 1972), and resulted in a classification of the flow behavior based on the height-to-spacing ratio of the ribs. Another study dealt with the effect of uneven rod height (Nagano et al., 2004). Bailon-Cuba et al. (2009), Ikeda and Durbin (2007) report on the effect of randomly distributed height of 2D roughness elements. 3D roughness elements were studied as well with DNS (Orlandi et al., 2006; Leonardi et al., 2003, 2007; Bhaganagar et al., 2004; Coceal and et al., 2006), including the effects of the Reynolds number and the spacing between elements.

However, numerical data for small roughness elements are limited. The numerical study presented in this paper investigates fully-developed turbulent flow over small hemispherical roughness elements at high Reynolds number; here 'small' means that the size of the roughness elements is of the order of the near-wall viscous boundary layer, which of course decreases at increasing Reynolds number. Data so obtained fill the gap between the smooth-wall data and other large-roughness results abundant in the literature. The availability of high performance computing facilities lifts the obstacle of inadequate resolution of the small roughness elements.

The interaction between the roughness elements attached to the wall and the streamwise vortices modifies the near-wall layer with respect to the case of a smooth-wall flow, for which the conventional 'law of the wall' applies:

$$U^+ = \frac{1}{\kappa}\ln y^+ + A \tag{1}$$

where U^+ and y^+ are the normalized velocity and length scale (turbulence wall unit) respectively, κ is the von Karman constant ($\sim$0.4), and A is the smooth wall constant ($A \sim 5.1$ for flow in a pipe). The $^+$ symbol indicates normalization. Velocity is normalized by the shear velocity $u_\tau \equiv \sqrt{\frac{\tau_w}{\rho}}$ and the normalized length scale is defined as $y^+ = \frac{u_\tau y}{\nu}$ (ν is the kinematic viscosity). In the rough wall regime, the velocity profile in the inner layer would be modified according to the following equation:

$$U^+ = \frac{1}{\kappa}\ln\left(\frac{y}{k}\right) + B(k^+), \quad B(k^+) = A - \Delta U^+ + \frac{1}{\kappa}\ln k^+ \tag{2}$$

ΔU^+ is the modification of the smooth wall constant due to roughness effects and is frequently called the roughness function. k is the wall-normal height of the roughness elements in meters. The shear Reynolds number is given as: $\mathrm{Re}_\tau \equiv \frac{hu_\tau}{\nu}$, where h is the half channel height. Also the friction coefficient is defined as:

$$f = \frac{8\tau_w}{\rho U_b^2} = 8\left(\frac{u_\tau}{U_b}\right)^2 \tag{3}$$

where U_b is the bulk fluid velocity.

3. Numerical procedure

3.1. Computational algorithm

The three-dimensional DNS and the LES simulations presented here were performed with the finite volume CFD/CMFD code TransAT©. A collocated, Cartesian grid was used and the incompressible Navier–Stokes equations were solved. The approach employed here is to represent the solid obstacles in a Cartesian mesh (rather than using a body-fitted grid). The method used (Labois et al., 2010) is a specific variant of the Immersed Boundary Method of Peskin (Peskin, 1977; Mittal and Iaccarino, 2005). In the present Immersed Surface Technique (IST), the solid object is captured in the Cartesian grid using a level set function; where the positive values denote the fluid domain, the negative values identify the solid domain and the surface of the wall is implicitly represented by the zero level set.

The fluid domain indicator function (derived from the level set function) varies smoothly across the wall surface with a support of two cells on each side of the fluid–solid interface. The no-slip condition at the wall is imposed through a relaxation term which acts as a distributed momentum sink reducing the fluid velocity as the indicator function goes to zero (Beckermann and et al., 1999).

The mesh was locally refined in the regions of interest, namely in the region right next to the walls extending into the wall-normal direction beyond the end of the roughness elements and up to the buffer layer. In those regions, the grid had two layers of ghost cells enabling the high resolution of the roughness elements ($\sim$10 grid points per element radius). Then, the meshed domain was decomposed into a number of blocks equal to the number of processors to be used for the calculation. Transfer of information between neighboring blocks was performed using MPI parallelization. All simulations were carried out using the 2nd order Central Difference scheme for the discretization of the convective fluxes. An explicit 3rd order Runge–Kutta scheme was used for the time integration. The time-step was adaptive and bound by a Courant number fixed between 0.1 and 0.3 to guarantee stability of the simulations. For the pressure–velocity coupling the SIMPLEC algorithm was used. The SIP preconditioned GMRES augmented by the use of the parallel PETSc solver library was used for the pressure solver.

In the LES simulations, the WALE subgrid scale model (Nicoud and Ducros, 1999) was used to account for the unresolved, subgrid-scale turbulence. This is a zero-equation model with features similar to Smagorinsky's model (Smagorinsky, 1963), albeit including the rate of change of vorticity in the definition of the eddy viscosity, besides the strain rate tensor.

All simulations were set up and post-processed on a local, 64 bit, 12-core workstation machine and run on hundreds or thousands of MPI-enabled processors in the Oak Ridge Leadership Computing Facility 'Jaguar', now called 'Titan'.

3.2. General simulation setup

In all simulations the domain consisted of a Cartesian box (Fig. 1), the size of which was selected to include the largest eddies in the flow and such that the turbulent eddies would not be correlated. Thus, for the smooth wall flow the Cartesian box had dimensions $L_x = 2\pi h$, $L_y = 2h$, and $L_z = \pi h$, where h is the half-channel height (wall-normal direction). h was kept constant in all our simulations. The streamwise and spanwise dimensions of the box were varied slightly between simulations in order to account for the different number of roughness elements or the increase or decrease in the spacing between roughness elements. Since fully developed turbulent channel flow is homogeneous in the streamwise and spanwise directions, x and z respectively, periodic

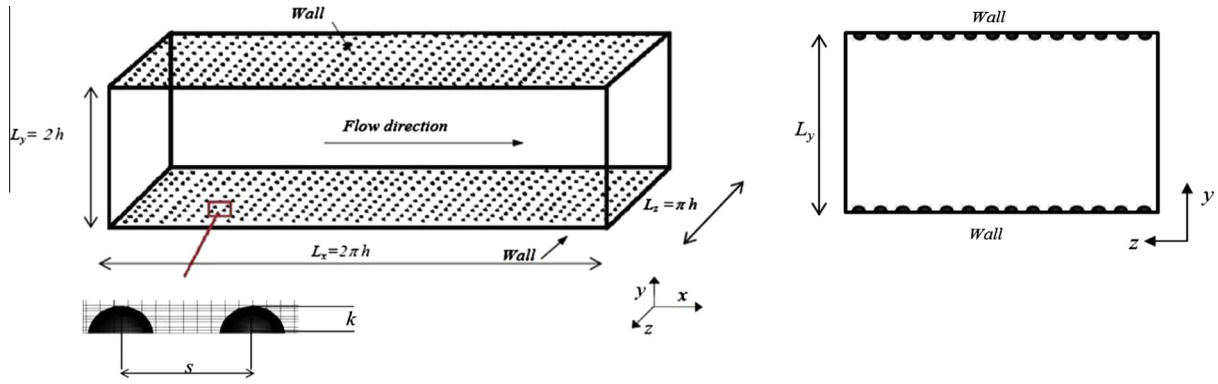

Fig. 1. Schematic of computational domain for roughened-channel flow simulations.

boundary conditions could be applied in these directions. No-slip boundary conditions were applied both on the upper and lower horizontal planes of the channel and on the roughness elements surface.

The shear Reynolds number Re_τ was set at 400 and 180. A pressure gradient source term was imposed in the x-momentum equation in order to achieve the imposed shear velocity, and thus the target shear Reynolds number. The shear velocity relates to the pressure gradient (dp/dx) in the following way:

$$u_\tau = \left(-\frac{h}{\rho}\frac{dp}{dx}\right)^{1/2} \tag{4}$$

For the coarsest LES simulation of rough wall channel flow, the flow field was initialized using a previously-run fine grid LES simulation of smooth turbulent channel flow with the same shear Reynolds number ($Re_\tau = 400$ or 180 respectively). For all subsequent simulations of rough wall channel flow, both LES and DNS, the coarsest rough-wall LES simulation velocity and pressure field were used to initialize the flow field.

Turbulent statistics were computed from solution samples, once statistically ergodic conditions were obtained. Space averaging was also performed in the streamwise and spanwise directions throughout the entire domain. More details are given separately with the presentation of each case.

4. Simulations

4.1. Overview

The following sequence of simulations and analyses was performed:

1. Smooth wall LES and DNS, including solution verification and validation.
2. LES of one representative hemispherical element case, including solution verification.
3. DNS simulations of one representative hemispherical element case.
4. Comparison of LES and DNS for the representative hemispherical element case.
5. LES parametric study for hemispherical roughness elements, with variation of the spacing between hemispheres, hemisphere height and Re_τ. LES with random hemispheres distributions, including random variation of the hemisphere sizes.

The simulation matrix is reported in Table 1.

4.2. DNS and LES of turbulent flow in smooth channel

4.2.1. DNS of smooth channel flow

Three DNS simulations were performed with increasingly finer meshes. The geometry and the boundary conditions are those described above in Section 3.2, identical in all three simulations. The streamwise and spanwise spatial discretization was uniform throughout the domain. However, the grid was refined near the wall in the wall normal direction. The minimum and maximum grid-cell values expressed in Δh^+ units can be seen in Table 2. A typical grid for these DNS simulations can be seen in Fig. 2. The refinement ratio between two consecutive grids is ($=\sqrt[4]{2}$), applied uniformly in the domain. The same scaling applies to both the number of processors used and the total number of cells for each simulation.

Turbulence was established relatively quickly; statistically steady (ergodic) conditions were reached before the collection of statistics started from individual flow fields for the total number of non-dimensional time steps ($t^+ = \frac{tu_\tau^2}{\nu}$) reported in the bottom row of Table 2. Space averaging was performed in the homogeneous streamwise and spanwise directions in order to increase the statistical sample.

The mean streamwise velocity for all three DNS cases is presented in Fig. 3. The streamwise wall-normal, spanwise and shear stresses are plotted in Fig. 4, which also includes two sets of DNS data: those of Krogstad and et al. (2005) for the same shear Reynolds number and those of Hoyas and Jimenez (2008) at $Re_\tau = 550$. It can be seen that the present DNS are in accord with

Table 1
Simulation matrix of LES and DNS cases.

	Smooth wall		Wall with hemispherical roughness elements							
			Regular distribution						Random distribution	
Simulation type	DNS	LES	DNS			LES				
Roughness size (k^+)	N/A		10	10	10	10	10	20	10	10–20
Spacing/size (s^+/k^+)			2	2	2	4	6	2	2	2
Re_τ	400, 180	400, 180	400	400	400, 180	400	400	400, 180	400	400

Table 2
Simulation characteristics and statistics collection parameters for DNS simulations of smooth wall channel flow.

		Grid 1 'vc' very coarse	Grid 2 'c' coarse	Grid 3 'f' fine
Number of nodes	x	256	304	362
	y	192	228	272
	z	192	228	272
Resolution	Δx^+	9.81	8.18	6.92
	Δy^+_{min}	0.91	0.76	0.67
	Δy^+_{max}	5.65	4.71	4
	Δz^+	6.54	5.45	4.65
Number of processors		480	800	1344
Number of cells (M)		9.3	15.6	26.3
Statistically steady state after (t^+)		12,000	18,000	16,800
Averaging performed after steady state for (t^+)		10,800	10,000	7200

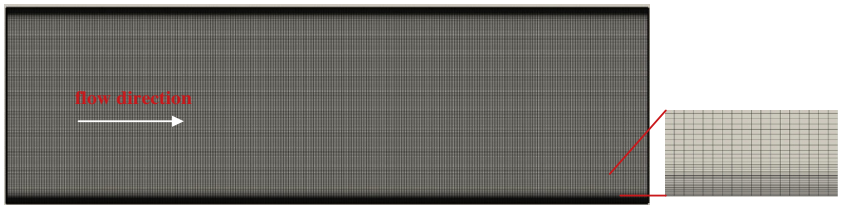

Fig. 2. Typical grid used for the DNS and LES smooth wall simulations.

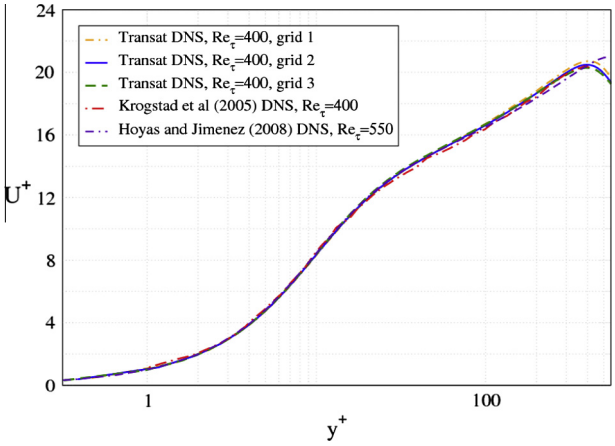

Fig. 3. Mean streamwise velocity from smooth wall DNS simulations ($Re_\tau = 400$).

the selected sets of published DNS, for the same order of shear Reynolds number.

4.2.2. LES of smooth channel flow

The LES equations are well known and so is the subgrid-scale (SGS) stress definition and modelling within the eddy viscosity context, linking linearly the SGS eddy viscosity to the gradients of the filtered velocity field. The WALE SGS model (Nicoud and Ducros, 1999) was employed in the present context; it defines the SGS eddy viscosity as follows:

$$\nu_t = (C_w\Delta)^2 \frac{(S^d_{ij}S^d_{ij})^{3/2}}{(\bar{S}_{ij}\bar{S}_{ij})^{5/2} + (S^d_{ij}S^d_{ij})^{5/4}} \tag{5}$$

where $C_w = \sqrt{10.6C_s^2}$ and S^d_{ij} reads:

$$S^d_{ij} = \frac{1}{2}(\bar{g}^2_{ij} + \bar{g}^2_{ji}) - \frac{1}{3}\delta_{ij}\bar{g}^2_{kk} \tag{6}$$

$$\bar{g}_{ij} = \frac{d\bar{u}_i}{dx_j} \quad \text{and} \quad \bar{g}^2_{ij} = \bar{g}_{ik}\bar{g}_{kj}$$

where δ_{ij} is the Kronecker symbol. In the current simulations, the Smagorinsky constant C_S is assigned the value of 0.08, and the filter width Δ is set equal to $2\Delta_{grid}$. The model has been shown to behave very well in wall-bounded flows, without a specific damping function similar to Van Driest's Van Driest (1956). It has also been shown to be less dissipative and able to capture the thin-shear layer accurately.

Three LES simulations were performed with increasing mesh refinement. The geometry and the boundary conditions shown in Fig. 1 were used also for these LES simulations. The grid was refined near the wall in the wall normal direction. The refinement ratio between two consecutive grids was $\sigma = \sqrt{2}$, applied uniformly in the domain. The simulation setup and statistics are presented in Table 3. The number of grid points was obviously lower than DNS, however the grid resolution near the wall approached that of the DNS.

The mean streamwise velocity for all three LES grids is presented in Fig. 5, along with the streamwise wall-normal, spanwise and shear stresses in Fig. 6. For comparison, the figures also report our DNS results. Note that the LES solution approached the DNS solution as the mesh is refined, which is the expected behavior. The accuracy of the LES was high even at low grid resolutions, as it predicted both the mean velocity and the stresses distributions well. The mean streamwise velocity value at the center of the channel had maximum and average deviations from the DNS solution of 3.5% and 1%, respectively. The convergence and the quality of the LES simulations are discussed in the Appendix.

4.3. DNS and LES of channel flow with hemispherical roughness elements

One DNS and three LES simulations of the turbulent channel flow case with hemispherical roughness elements were performed. The geometry and boundary conditions are those shown in Fig. 1. The BMR (short for Block Mesh Refinement) technique was used in all hemispherical roughness elements cases to resolve the wall layer containing the roughness elements in order to alleviate the resolution limitations of simple, single-block refined grids as used in the smooth cases (Fig. 2). The BMR gridding is shown in Fig. 7. A

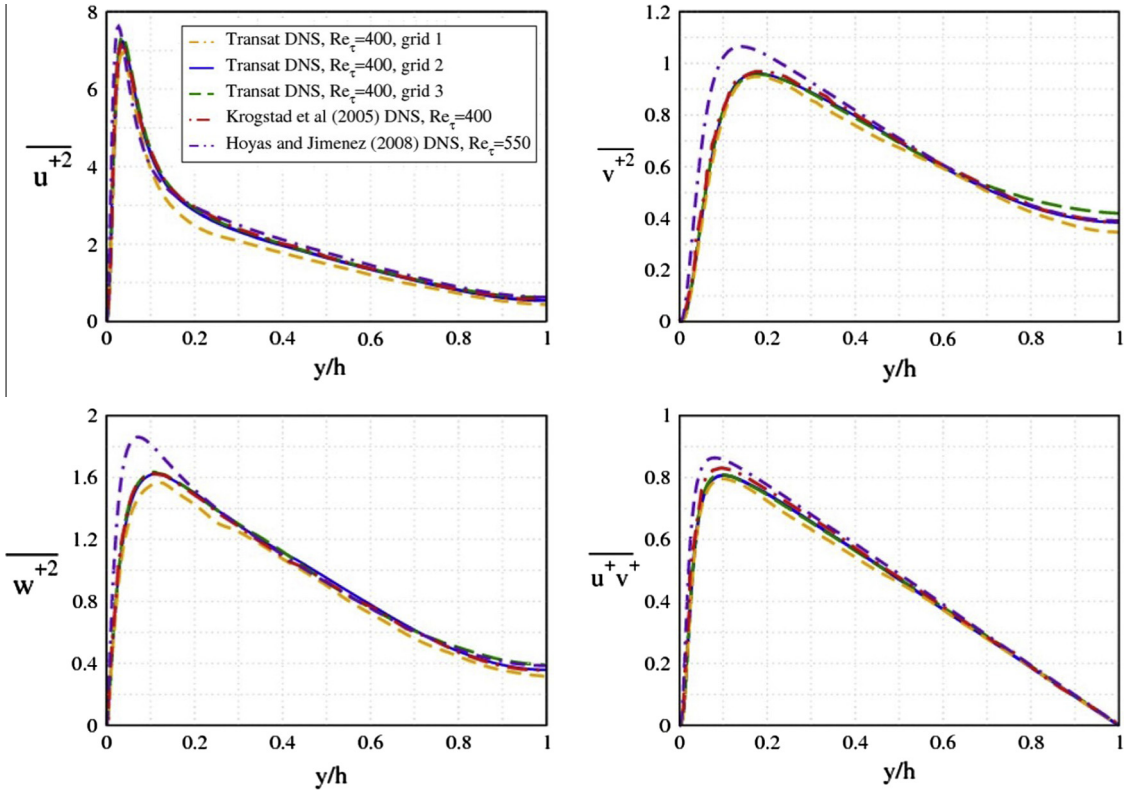

Fig. 4. Streamwise, wall-normal, spanwise and shear stresses from smooth wall DNS simulations ($Re_\tau = 400$).

Table 3
Simulation characteristics and statistics collection parameters for LES simulations of smooth wall channel flow.

		Grid 1 'vc' very coarse	Grid 2 'c' coarse	Grid 3 'f' fine
Number of nodes	x	91	128	181
	y	68	96	136
	z	68	96	136
Resolution	Δx^+	27.74	19.61	13.87
	Δy^+_{min}	2.56	1.81	1.28
	Δy^+_{max}	16.00	11.31	8.00
	Δz^+	18.48	13.07	9.24
Number of processors		24	60	168
Number of cells (Million)		0.4	1.2	3.3
Statistically steady state after (t^+)		40,000	20,000	12,000
Averaging performed after steady state for (t^+)		24,400	18,400	10,800

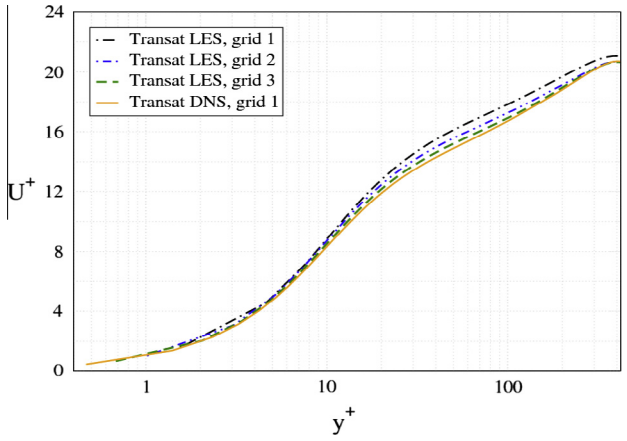

Fig. 5. Mean streamwise velocity profile from smooth wall LES simulations, compared to DNS of the same case ($Re_\tau = 400$).

uniform coarse grid was used as the first layer and a refined grid was superimposed to that first layer covering the region starting from the wall and up to $y^+ \sim 40$ (applied to both walls). The refined layer featured a gradually decreasing resolution in the y-direction while in the x- and z directions the resolution was fine yet uniform.

Beyond $y^+ \sim 40$ the resolution was decreased towards the center of the channel with the mean grid size increasing from the near wall region ($\Delta^+_{min} = 2.4$-DNS case) to the mid channel plane ($\Delta^+_{max} = 7.6$-DNS case). Both the minimum and the maximum mean grid sizes satisfy the criterion for sufficient grid resolution (Groetzbach, 1983). That criterion dictates that the average Δ^+ should be lower than $\pi\eta^+$. In our case, the non-dimensional Kolmogorov lengthscale was $\eta^+ \sim 4.5$. The simulation characteristics along with the averaging details and the statistics are reported in Table 4 both for LES and DNS.

Space averaging is performed over the entire domain, both in x and z directions while excluding the regions obstructed by the hemispheres. Therefore, a single representative y-distribution for

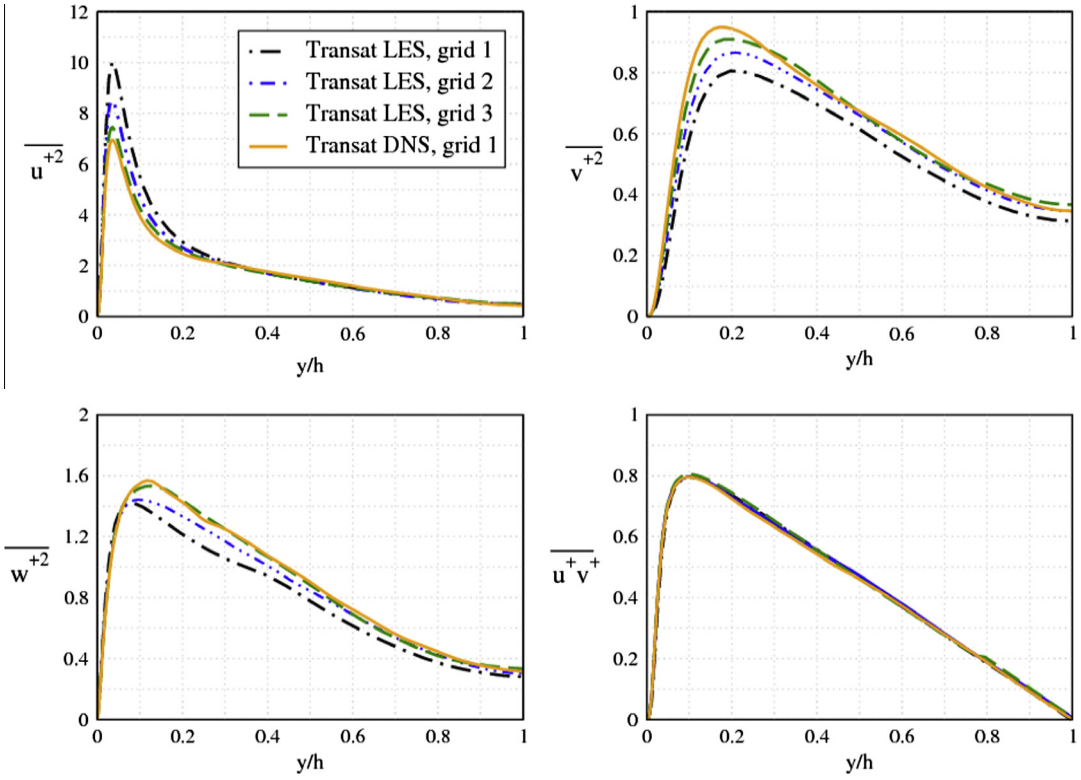

Fig. 6. Streamwise, wall-normal, spanwise and shear stresses from smooth wall LES simulations, compared to DNS of the same case ($Re_\tau = 400$).

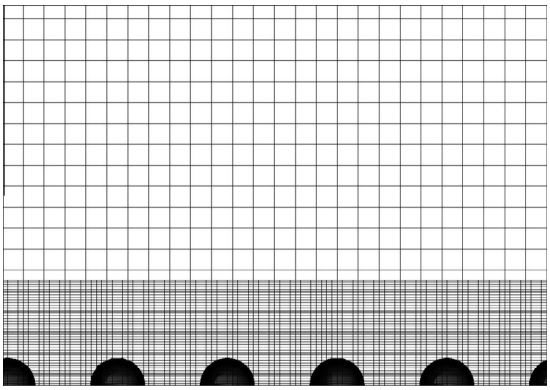

Fig. 7. Block Mesh Refinement (BMR) technique used for rough wall LES and DNS simulations.

velocity and Reynolds stress can be shown. However, it is interesting and important to analyze also the flow structure locally, in the vicinity of the hemispherical roughness elements. Data was extracted from our DNS simulation results for several x–z locations, as shown in Fig. 8. Position A was on the top of the obstacle whereas all other positions were in between obstacles.

The data extracted were the mean velocity profiles (only time averaged) in the y-direction, and are shown in Fig. 9, using inner scaling. Note that the mean velocity profiles for the cases with hemispherical obstacles, a downward shift from the smooth wall solution was observed, since the drag created by the obstacles slows down the flow (for the same imposed pressure gradient). The shift was constant in the outer flow region ($\Delta U^+ \sim 2$), which was way lower than what has been observed in other studies dealing with larger obstructions in which ($\Delta U^+ \sim 7$–9). However, a close inspection of the profiles suggested that this behavior was clearly dependent on the sampling location: while right at the top of the elements, the shift was complete, at other in-between locations (B, C, D) the flow exhibited transition mechanisms from smooth to rough scenario, with a gradual destruction of the viscous sublayer. It is noted that in Fig. 9, the origin of y^+ (or point where y^+ is 0) is always the boundary corresponding to the wall without the obstacles. As a result, the curve corresponding to point A starts from $y^+ = 10$.

On average, the velocity profiles should exhibit a roughness-induced structure similar to that of Fig. 10. The streamwise mean velocity profiles obtained with both LES and DNS are presented in Fig. 10 against wall units, and are compared to the log-law. The normal and shear stresses are plotted in Fig. 11, using outer scaling (y/h), which is the practice for grid and model convergence studies. As expected, the LES solution approached indeed the DNS solution as the mesh was refined. The accuracy of the LES was rather high for such a complex geometry even at low grid resolutions (comparing to DNS; 7.6 million cells vs. 23 million cells; actually convergence was already attained for Grid 2 LES); both the mean velocity and the stresses were well predicted. The profiles clearly depicted a drag enhanced flow induced by the presence of the roughness elements, eliminating the viscous-layer flow features ($y^+ < 11.6$) from the picture.

Let us now turn to the comparison of the smooth and rough cases. For this purpose we used the finest LES grid (Grid 3) results only. While it was clear that the inner scaling applied to the mean velocity profile exhibited a downward shift, it was interesting to address the universality of that shift and its dependence on the roughness elements. The mean velocity defect can be expressed as $\Delta U^+ = (U^+ - U_{Cl})$ where U_{CL} is the centerline velocity. When plotted in outer scaling (vs. y/h), ΔU^+ for $Re_\tau = 400$ showed a perfect overlap in the outer flow region (Fig. 12a), meaning that either the shift function is universal or the velocity characteristics were

Table 4
Simulation characteristics and statistics collection parameters for DNS and LES simulations of hemispherical roughness channel flow (using the BMR meshing method).

		LES			DNS
		Grid 1	Grid 2	Grid 3	
Coarse layer					
Number of nodes	x	157	176	199	330
	y	50	57	64	106
	z	79	88	100	166
Resolution	Δx^+	15.9	14.2	12.7	7.6
	Δy^+	15.9	14.2	12.7	7.6
	Δz^+	15.9	14.2	12.7	7.6
Fine layer (superimposed to coarse)					
Number of nodes for each of the two walls	x	467	524	594	659
	y	15	17	19	41
	z	234	261	298	331
Resolution	Δx^+	5.32	4.75	4.24	3.8
	Δy^+_{min}	2.66	2.34	2.1	0.93
	Δz^+	5.32	4.75	4.24	3.8
Total number of cells (Million)		3.6	5.2	7.6	23.1
Number of processors		176	320	432	1200
Statistically steady state after (t^+)		11,200	12,800	12,000	12,000
Averaging performed after steady state for (t^+)		16,800	11,600	12,800	6000

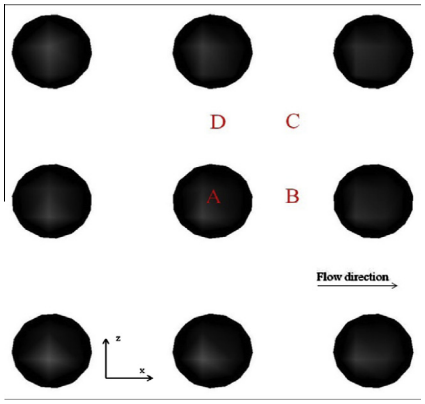

Fig. 8. Locations of data extraction on x–z plane.

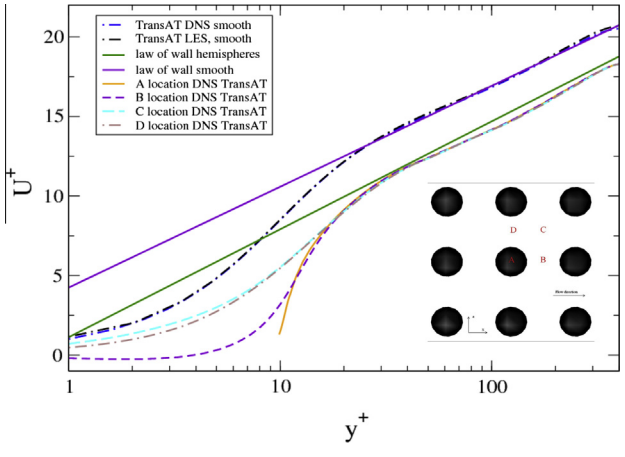

Fig. 9. DNS mean velocity profiles for $s/k = 2$ for the locations shown in Fig. 8. Comparison with smooth wall velocity profile and law of the wall.

independent of surface geometry in the outer region, which is consistent with Townsend's (Townsend, 1976) Reynolds number similarity hypothesis. Inner scaling (Fig. 12b), however, suggests that the shift function is not universal in the inner layer. We thus

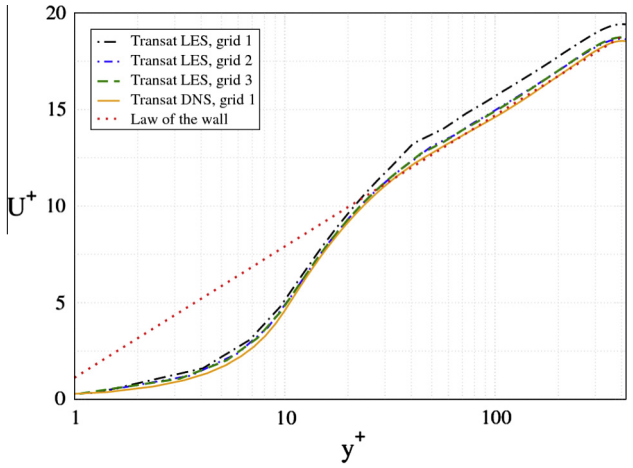

Fig. 10. Mean streamwise velocity profiles for LES simulations of hemispherical roughness case, compared with DNS of the same case.

concluded that the Reynolds number similarity hypothesis could be justified only in the outer layer, and thus the velocity characteristics were somewhat dependent on the surface topology.

While the outer-scaling plots of the stresses (Fig. 13a) did not show substantial differences, the inner-scaling plots revealed some interesting findings as to the effect of roughness on turbulence, interpreted broadly (Fig. 13b). The vertical fluctuating stresses seemed to be unaffected by the presence of roughness elements. The fluctuating field decayed as the wall (smooth or rough) was approached in a similar way. The most important finding was that the rate of momentum transfer from the mean flow to the streamwise fluctuating field, and thus $\langle u'^2 \rangle$ reduced in effect compared to the smooth case by about 10%, with the peak location sliding towards the outer layer by about $\Delta y^+ = 10$. Conservation of momentum and energy requires that the losses be absorbed by another component: the $\langle w'^2 \rangle$. The peak location for this quantity was now shifted back. Below $y^+ = 11$, all energy components were drastically weaker than in the smooth case, apart from the vertical stress, where the similarity of the decay of turbulence was clearly independent of the surface topology.

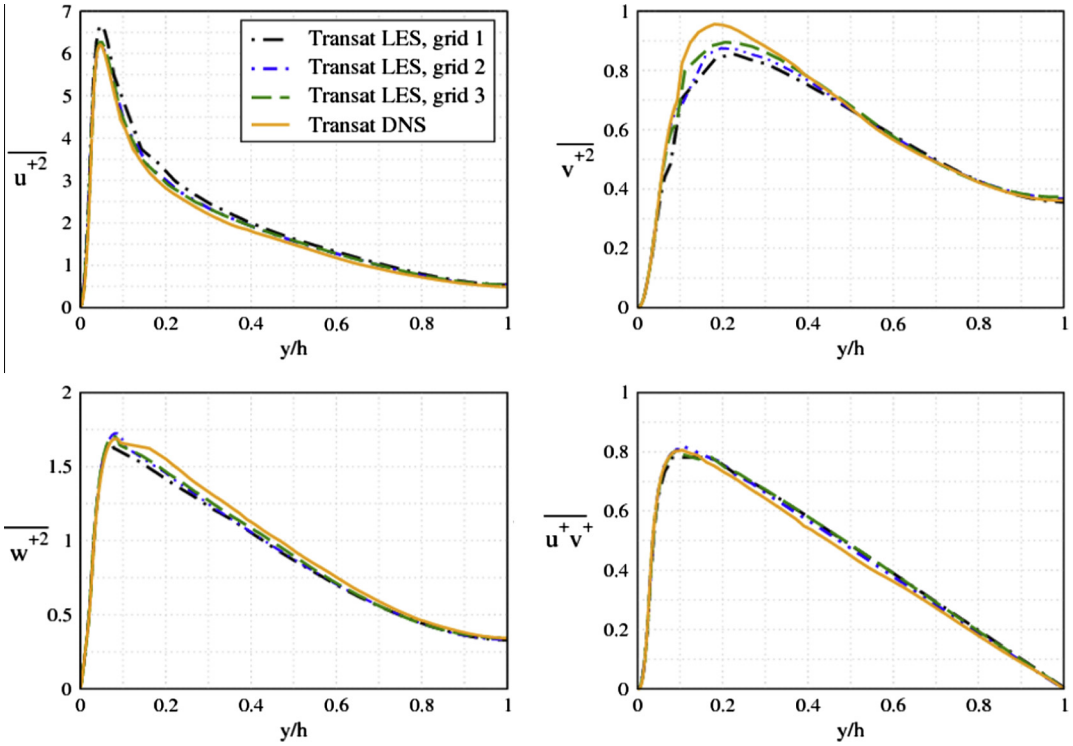

Fig. 11. Streamwise, wall-normal, spanwise and shear stresses profiles for LES of hemispherical roughness case, compared with DNS of the same case.

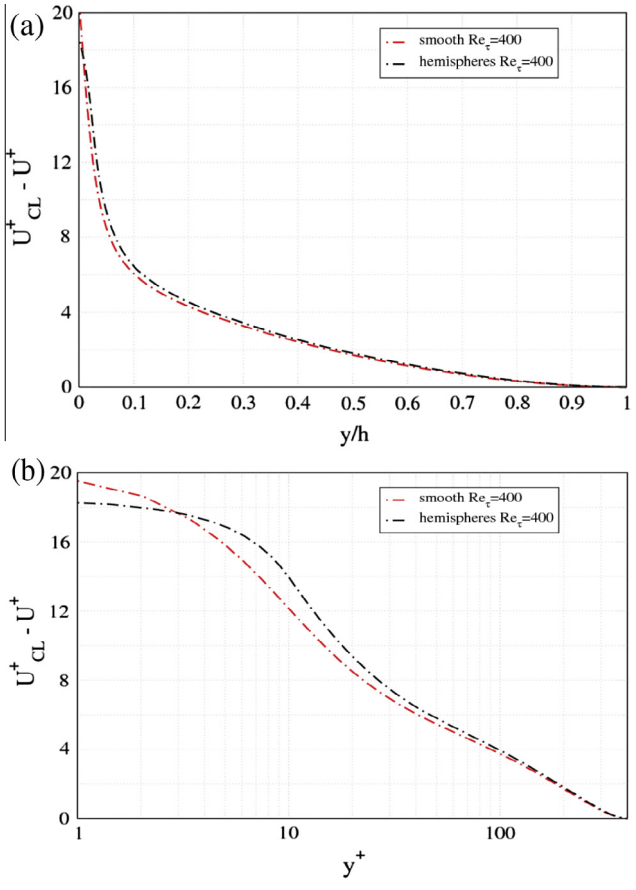

Fig. 12. Velocity defect in (a) outer scaling and (b) inner scaling.

Also, the turbulent kinetic energy (TKE = 1/2 ($\langle u'^2\rangle + \langle v'^2\rangle + \langle w'^2\rangle$)) profiles for the case of hemispherical roughness elements and the smooth wall case can be seen in Fig. 14. The TKE levels were lower near the wall for the rough case, while they did not seem to differ in the middle of the channel. That is due to the flow slowdown in the streamwise direction. This means that there was a clear cut between the inner and outer layer in this case, a feature observed also with other types of roughness elements (Krogstad et al., 2005; Leonardi et al., 2007). The behavior of TKE is in fact similar to the streamwise stress component, which contributes most to TKE.

The sources of energy transfer between the three turbulent stress components can only be revealed through a detailed analysis of the source terms in the Reynolds stress budget. Looking solely at the production of turbulence kinetic energy term may be either misleading in the 3rd direction-flow-homogeneity assumption or may hide other important subtle mechanisms.

The pressure diffusion source term provides a better and more straightforward way to explain the inter-component energy redistribution observed in Fig. 13. The term provides a source of energy and a contribution mechanism to redistribute it. The energy redistributive part called the pressure-rate-of-strain tensor and defined as (Perry et al., 1969)

$$R_{ij} = \overline{\frac{p}{\rho}\left(\frac{\partial u_i'}{\partial x_j} + \frac{\partial u_j'}{\partial x_i}\right)} \tag{7}$$

serves in effect to redistribute energy among the Reynolds stresses promoting isotropy of turbulence. By virtue of continuity, the trace of R_{ij} is zero, and consequently this term vanishes in the transport equation of the turbulent kinetic energy. Each term of the trace of R_{ij} is then used to define the pressure-strain correlation,

$$R_{ii} = \overline{\frac{p}{\rho}\left(\frac{\partial u_i'}{\partial x_i}\right)} \quad i = 1,2,3 \tag{8}$$

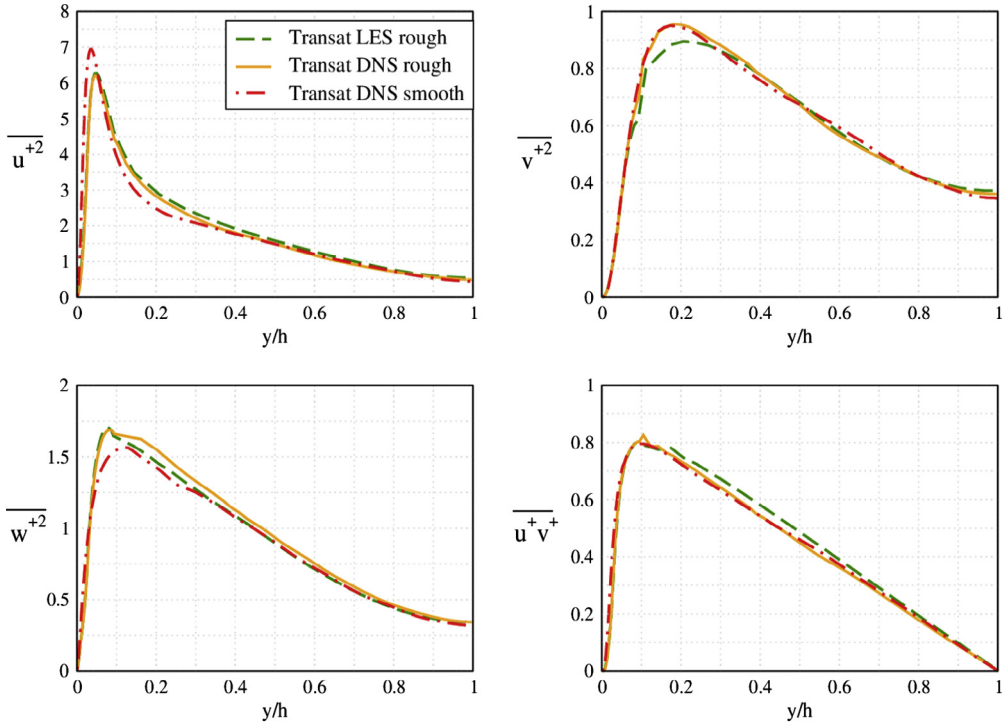

(a) Plots in outer scaling

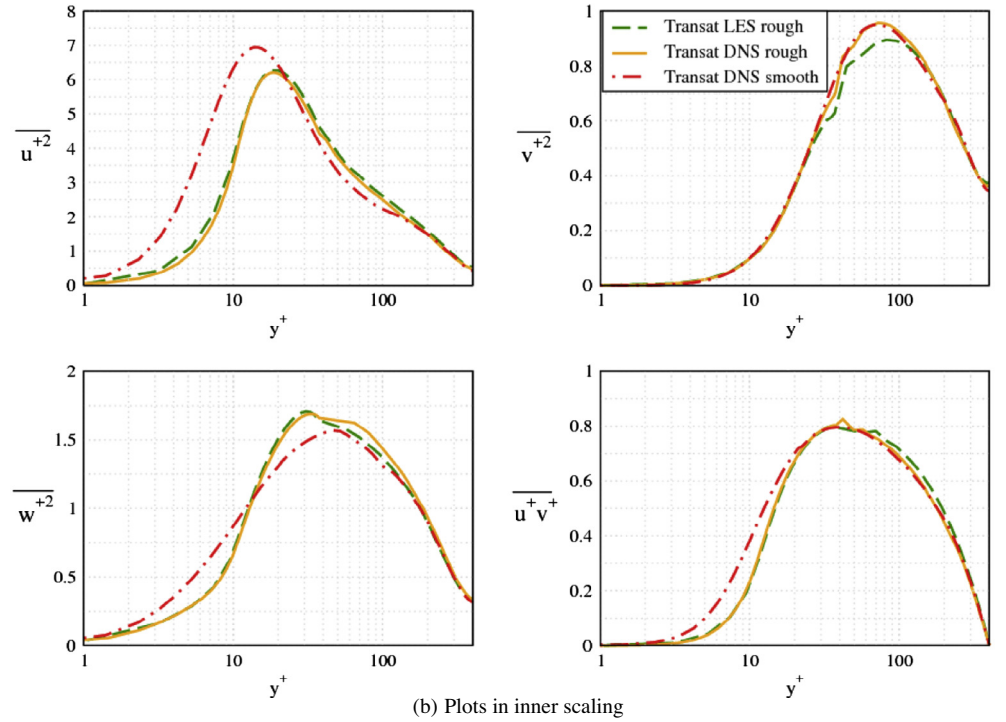

(b) Plots in inner scaling

Fig. 13. Streamwise, wall-normal, spanwise and shear stresses profiles for LES and DNS of rough-wall case compared with DNS of the smooth-wall case.

a positive value of which implies a transfer of energy into component i from the other components, and vice versa. The transfer of energy from $\langle u'^2 \rangle$ to $\langle w'^2 \rangle$ observed in Fig. 13 can only by explained by R_{33} being >0, reflecting the occurrence of local, instantaneous bulging flow in the third direction induced by the roughness elements, thus $\frac{\partial w'}{\partial z} > 0$.

Contours of the instantaneous streamwise velocity in the entire domain are shown in Fig. 15a while Fig. 15b shows the instantaneous velocity contours at a slice in the middle of the hemispheres, as those where computed from the DNS simulation. The recirculation regions in between the hemispheres are also featured in the same figure. The flow was shown to penetrate the roughness layer

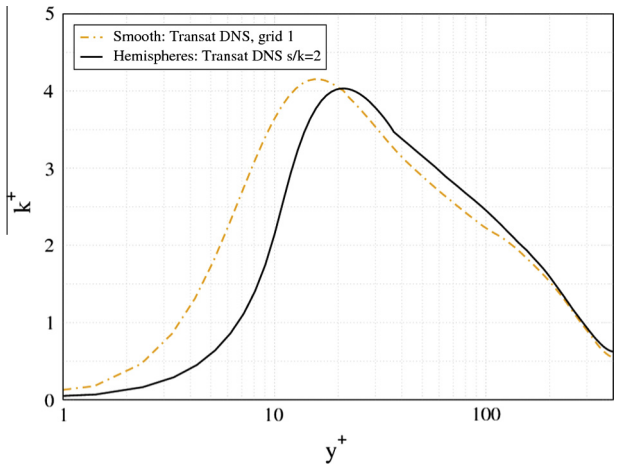

Fig. 14. Turbulent kinetic energy distribution in the spanwise direction for rough and smooth wall DNS.

with negative momentum sucking towards the wall, thus inducing inter-element flow recirculation.

A further insight into the wall layer and the effect of the wall roughness on the flow structure could be gained by looking at the instantaneous flow structures in the vicinity of the roughness zone. Fig. 16 compares the patchy quasi-coherent structures in the smooth case and rough case (for $k^+ = 10$ and $s^+ = 2$) at different heights from the wall: at $y^+ = 5$, 10, 15, 20, 25 and 30. Unlike previous similar studies, where the large square obstructions placed perpendicular to the flow direction caused large differences between the smooth and the rough wall flow structures (Ashrafian et al., 2004), here we observed one important phenomenon worth reporting, that is: the coherent structures controlling the drag were rather similar to the smooth case (at least for this roughness configuration, spacing and height) but were lifted up by almost a constant wall-unit shift y^+ (~10–15), which, interestingly, corresponds to the relative roughness $k^+ = 10$.

As explained in Section 2, the effect of the roughness elements on the flow is to shift the mean velocity profile by ΔU^+ with respect to the mean velocity profile of a smooth wall.

The friction factor can be extracted from the simulations using Eq. (3) and then compared to the friction factor estimated from Moody's diagram (or equivalent correlations). In the smooth wall case, the channel Reynolds number was approximately 29,000 (both for LES and DNS with small deviations). For this value of the Reynolds number, Moody's diagram gives a friction factor value of ~0.024, whereas our LES and DNS simulations plateaued at 0.025, as shown in Fig. 17.

The friction factor for the case with hemispherical roughness elements, extracted from the DNS and LES simulations, is shown in Fig. 18. It plateaued at about 0.0324, which is higher than the smooth wall case, as expected. The relative roughness (i.e. ratio of height of hemispherical obstacles to the channel hydraulic diameter) is 0.00625 and the Reynolds number is 25,100 for the DNS simulation. For this input, Moody's diagram gives a friction factor of 0.0355. The two values are within 8%, so Moody's diagram actually does a reasonable job at predicting the friction factor for our hemispherical roughness case. Note that the fine-grid LES simulation predicted a friction factor that is very close to the DNS-predicted value, again confirming the high quality of our LES approach despite the fact that the number of cells is less than 1/3 that of the DNS (LES: 7.6 million vs DNS: 23 millions).

5. LES parametric study of hemispherical roughness elements effects

The effect of roughness elements on the mean velocity, wall shear stress and friction factor is expected to depend on the shape, size, pattern and spacing of the elements, as well as on the Reynolds number. There have been several studies in the literature investigating the nature of this dependence. The most relevant ones to our study are summarized in Table 5. To the best knowledge of the authors, the present study is one of the few that address the effect of randomness of roughness distribution, and compare it to the case of a square lattice distribution.

To study such effects parametrically, the simulations summarized in Table 4 were performed using the LES approach. The reference case described in the previous section was used as a baseline for comparison. The mesh used in all the LES simulations of this parametric study was the same and it was the finest LES mesh used in the analysis in Section 4.3, which was proven to return results close to DNS.

In this section, the averaging procedure has been performed both in time and in space; the latter was performed throughout the entire domain by averaging the values of the points at the same y-location only. Finally, a time and space averaged velocity was produced starting from the wall of the channel ($y^+ = 0$), not the top of the obstacles.

5.1. Reynolds number effect

The reference case simulated in Section 4.3 had a friction Reynolds number $Re_\tau = 400$. To examine the effect of Reynolds number on the flow, we simulated the case of turbulent channel flow with

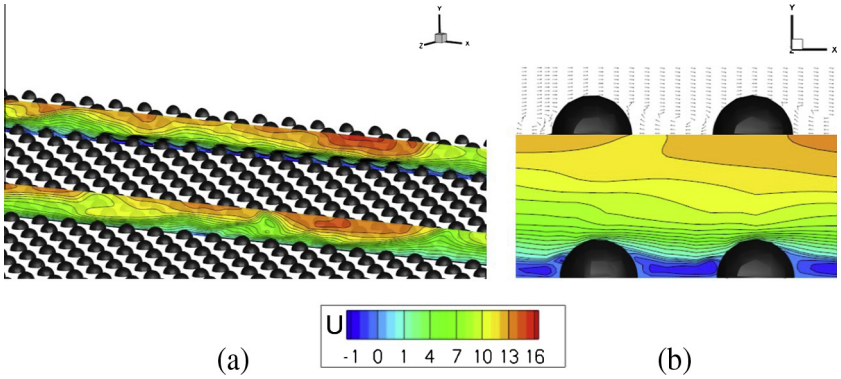

Fig. 15. (a) Instantaneous streamwise velocity contours for slices at the hemispheres crest and in between hemispheres. (b) Instantaneous velocity contours at a slice in the middle of the hemispheres. The recirculation regions in between the hemispheres can be clearly seen.

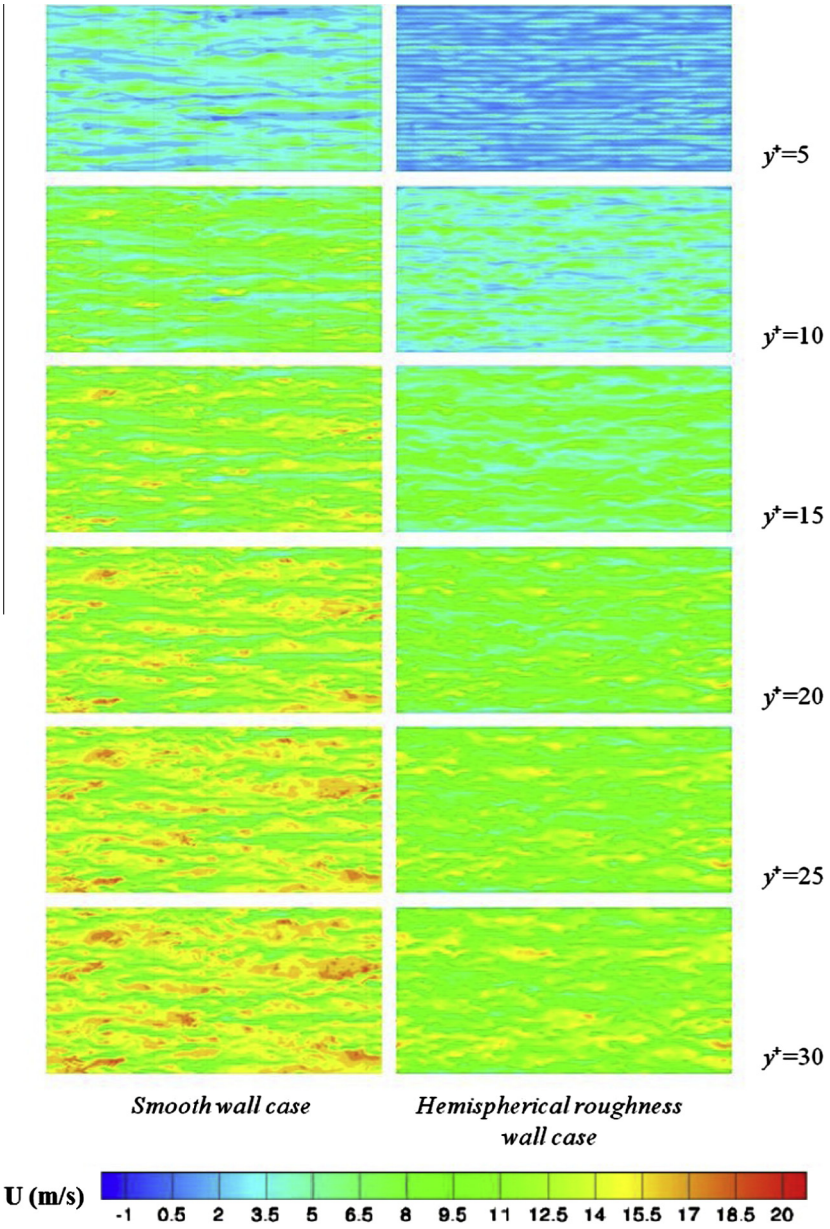

Fig. 16. Smooth wall (left) and hemispherical obstacles wall (right) instantaneous streamwise velocity contours at various y^+ locations from the wall. Planes parallel to the wall.

$Re_\tau = 180$. There is relevant data in the literature for this value of the Reynolds number and thus we could compare our results to other published data (Krogstad et al., 1992; Ashrafian et al., 2004). Also, the same grid resolution could be adopted for the lower Reynolds number, without loss of accuracy. We performed this simulation for both smooth and rough wall conditions. The comparison of the mean flow results can be seen in Fig. 19. It can be seen that the law of the wall is independent of the Reynolds number for the smooth wall, as expected. For the rough cases, the similarity of the log law is preserved (obviously at $y^+ > 10$) with the same lower velocity defect ΔU^+ as compared to the smooth cases (with the slope k remaining roughly unchanged (Table 6)), but with marked deviations in the region very close to the wall ($y^+ < 10$). Both phenomena were explained previously, the lower shift in the core flow region and transition mechanism in the viscous-affected layer. In particular, as the shear Reynolds number increases, the resistance caused by the roughness elements increases, too, meaning that the flow separates on the roughness surfaces earlier and more abruptly. This is in line with the statement put hitherto: in contrast to square-type roughness where the flow separates naturally at the edges, in this case there is a Reynolds number effect in the viscosity-affected layer.

5.2. Size effect

In order to investigate the effect of the roughness size, a case with hemispherical elements of double the size of the reference elements (but with same center-to-center spacing) was simulated. The effect in the downward shift of the mean velocity was significant and the friction factor increased by almost 36% with respect to the reference case (Fig. 20). This is consistent with the Moody's diagram prediction: doubling the roughness increases

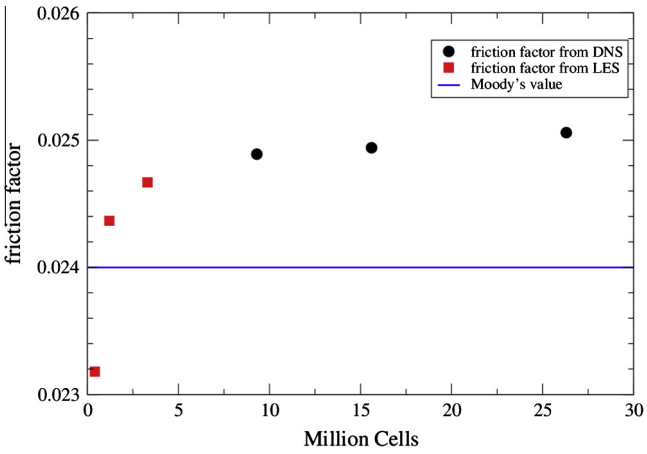

Fig. 17. Friction factor as a function of the number of cells for DNS and LES studies for smooth wall case. The solution actually converges at around 10 million cells already.

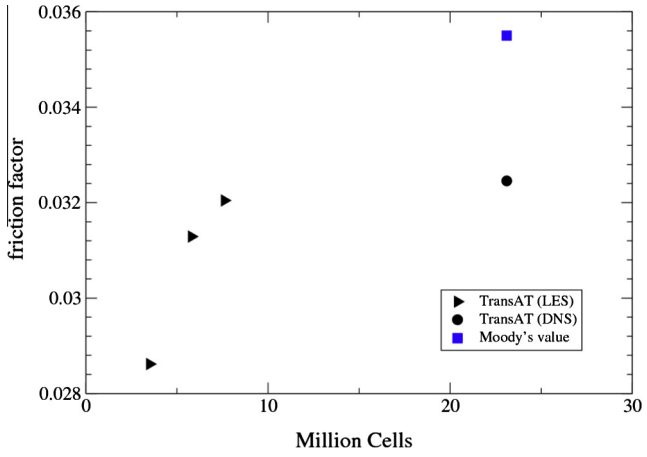

Fig. 18. Friction factor as a function of the number of cells for DNS and LES studies for hemispherical roughness elements and comparison with Moody's value.

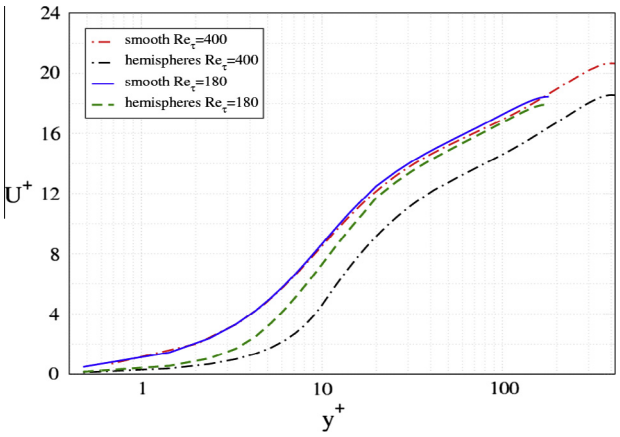

Fig. 19. Mean streamwise velocity for cases of smooth $Re_\tau = 400$, smooth $Re_\tau = 180$, rough $Re_\tau = 400$, rough $Re_\tau = 180$.

the friction factor by about 2.5. The main conclusion to draw here is that increasing the relative roughness k^+ shifts the log law further into the core flow.

5.3. Spacing effect for regular roughness distribution

The effect of spacing between roughness elements has been studied extensively in the literature, though for square type of roughness mainly. A common classification is that of *k*-type ('loose' spacing) and *d*-type ('tight' spacing) roughness, per Perry et al. (1969). For *k*-type roughness, eddies with length scale of order *k* are shed into the flow above the crests of the elements. For a *d*-type roughness, stable vortices form within the grooves and there is no eddy shedding into the flow above the elements. Transitional roughness is intermediate between *k* and *d*-types (Leonardi et al., 2007). However, this classification was developed for square cross section elements, and may not apply to hemispherical elements for the reasons explained earlier: flow separation is very sensitive and dependent on the wall curvature. Therefore, the effect of spacing on hemispherical elements was studied for cases with $s/k = 2$, 4

Table 5
Summary of previous and current work on rough channel flow.

	k^+	h/k	Random distribution	Shape (2D, 3D)	Variable size	Simulation type	Re_τ
Krogstad et al. (2005)	10	29.4	–	Square ribs (2D)	–	DNS	400
Leonardi et al. (2007)		10	–	Square ribs/triangular ribs (2D)	–	DNS	180, 480, 600
This study	10–20	40	Yes	Hemispheres (3D)	Yes	DNS/LES	180, 400

Table 6
Parametric simulation matrix and summary of main findings.

	Smooth		Hemispherical elements cases						
			Square lattice distribution					Random lattice	
Roughness size (k^+)			10	10	10	10	20	10	10–20
Spacing/size (s/k)			2	2	4	6	2	2	2
Re_τ	400	180	400	180	400	400	400	400	400
Friction factor	0.025	0.032	0.033	0.035	0.030	0.029	0.044	0.034	0.041
% Change from smooth wall case			30	7	21	15	79	37	66
ΔU^+			3.33	0.9	2.33	1.64	6.11	3.08	5.16
A	4.26	5.05	0.96	4.15	1.93	2.62	−1.85	1.18	−0.9
κ	0.36	0.38	0.34	0.37	0.34	0.35	0.32	0.35	0.33

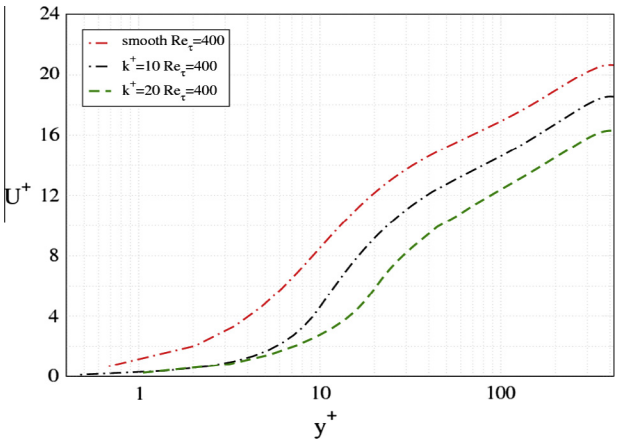

Fig. 20. Mean streamwise velocity for $Re_\tau = 400$ and two different roughness sizes: $k^+ = 10$ and $k^+ = 20$.

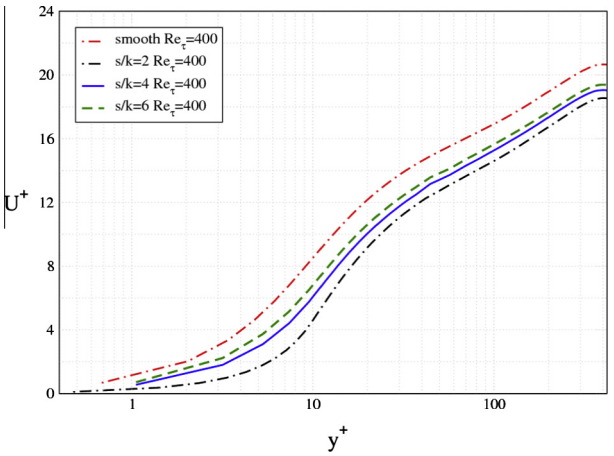

Fig. 22. Mean streamwise velocity for $Re_\tau = 400$ and three different cases: $s/k = 2$, $s/k = 4$, $s/k = 6$.

and 6. The contour plots of the instantaneous velocity for these three cases can be seen below in Fig. 21.

The size of these recirculation regions scales with the size of the elements, or the relative roughness. On the other hand, larger spacing seems to enhance momentum transfer from the core flow towards the wall; shorter spacing tends to homogenize the flow in the wall layer.

There was a modest difference between the three cases, with the mean velocity profile (Fig. 22) and the friction factor (Table 6) approaching the smooth wall values with increasing spacing, as expected. The log law similarity is perfectly preserved. Unlike *d*-type square-shaped roughness elements, here for the lowest $s/k = 2$ there was detachment and reattachment of the flow between two adjacent hemispherical obstacles.

5.4. Effect of random spheres distribution and variable spheres size

The effect of the spatial distribution (pattern) of the roughness elements was also investigated. A random distribution pattern was implemented, with the constraint of a minimum distance between elements of at least $s^+ = 20$. The instantaneous velocity contour plot along with the hemispheres distribution can be seen (Fig. 23) for $k^+ = 10$ and $10 < k^+ < 20$, while the friction factor is reported in Table 6.

The turbulent flow field is seen to be well established in both cases, featuring a similar structure to the non-random roughness distribution. The details of the flow in the vicinity of the roughness layer cannot be seen. The random distribution has a modest effect on the friction factor, which increases by about 3% as compared to the regular lattice case for the same spacing and Re_τ; by contrast, increasing the relative roughness from 10 to 20 increases the friction coefficient from 0.034 to 0.041, i.e. about 22%, which is not negligible.

Further, the effect of varying roughness elements sizes was also investigated for the (same) random spacing pattern to complete the analysis. The sizes were normally distributed in the range $10 < k^+ < 20$. The resulting averaged velocity profiles can also be seen in Fig. 24, and again in Table 6 as to the friction factor. The value of the friction factor for this case is lower than the case of random large obstacles, as expected. The figure shows that for $k^+ = 10$, regular versus random roughness distributions present the same behavior: a downward shift in the velocity profile, retaining the log law structure at the expense of washing out of the viscous sublayer. Increasing the relative roughness to $k^+ = 20$ shifts further

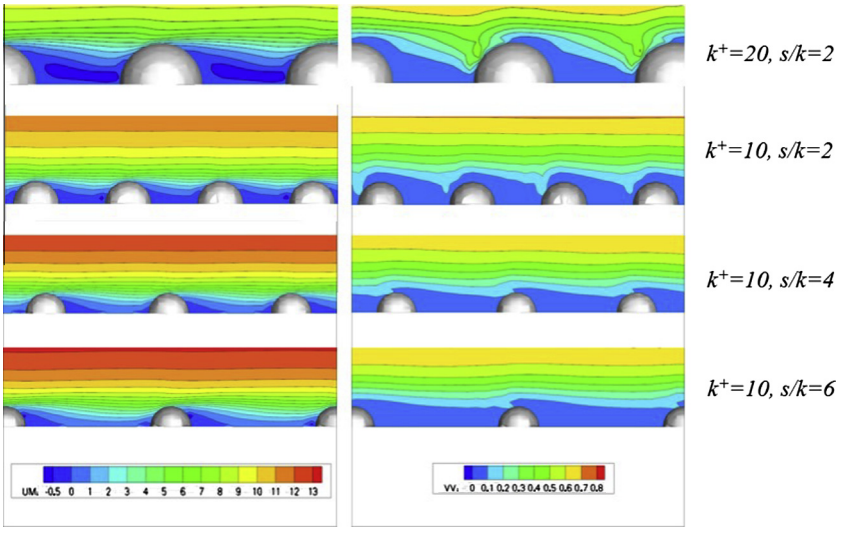

Fig. 21. (left) Time averaged streamwise velocity contour plots and *v'* contour plots (right) for four cases with different spacing and size of the hemispheres.

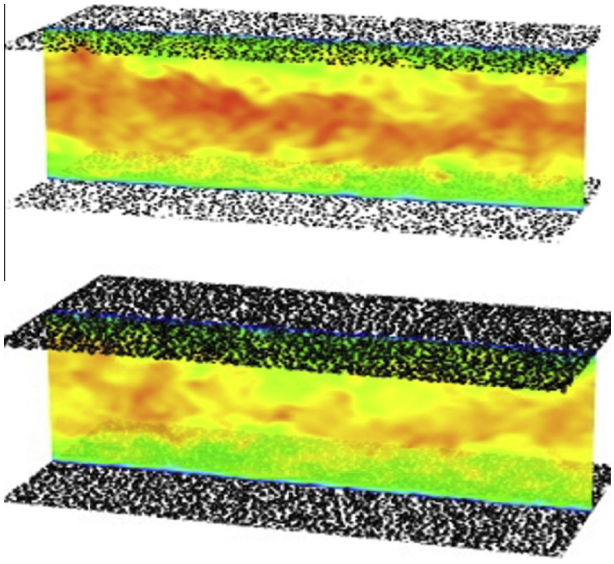

Fig. 23. Instantaneous streamwise velocity contour plots for the case of random spheres distribution. Upper plot: $k^+ = 10$, Lower plot: $10 < k^+ < 20$.

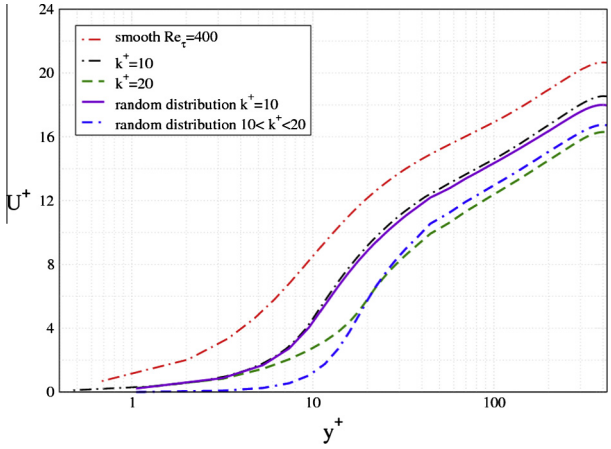

Fig. 24. Mean streamwise velocity for $Re_\tau = 400$ and four different cases: square pattern with $s/k = 2$ and $k^+ = 10$ and $k^+ = 20$, and random lattice with $k^+ = 10$ and $10 < k^+ < 20$.

down the preserved log profile away from the wall, at the same time pushing its validity further up; $y^+ > 30$.

The effect of increasing roughness height elements from $k^+ = 10$ to $k^+ = 20$ is seen in Fig. 24, where the smooth data are included for reference as well. Note that the case of $k^+ = 10$ with a random distribution does not show any difference with the regularly spaced case, and thus it is not included in the graph. As discussed previously in the context of Fig. 13, increasing roughness height causes a transfer of energy from the streamwise component to the lateral one; the phenomenon seems to be pronounced with increasing roughness height, but is independent of their distribution.

6. Conclusions

A detailed simulation campaign based on LES and DNS to investigate of the effect of hemispherical roughness elements on fully developed turbulent flow between parallel plates was presented here. Variations in the shear Reynolds number ($Re_\tau = 180–400$), element height ($k^+ = 10–20$), element spacing ($s^+/k^+ = 2–6$) and distribution pattern (regular square lattice vs. random pattern) were explored to assess their effect on the friction factor and mean velocity and turbulent stresses profiles. The present LES/DNS campaign differs from the abundant published works centering on large sharp-edged roughness obstructions ($k^+ = 40–100$), in that it deals with the transitional roughness regime, where the Reynolds number is relatively high (for a DNS), and the roughness elements are small and of round shape, and could thus be randomly distributed.

Overall the DNS results show a clear separation between the inner wall-layer, which is affected by the presence of the roughness elements, and the outer layer, which remains relatively unaffected. Roughness element height has a strong effect on the friction factor and on the mean velocity profile. The friction factor increases proportionally to the roughness element height, while the mean velocity profile shifts downward proportionally to the roughness element height. The type of roughness dealt with here also affects the turbulent stresses. In particular, the study reveals that the presence of roughness elements of this shape promote locally the instantaneous flow motion in the lateral direction in the wall layer, which was found to cause a transfer of energy from the streamwise Reynolds stress to the lateral component; the wall-normal stress component remains however unaffected regardless of the roughness height or arrangement. Consequently, the shape of the turbulent kinetic energy profile changes, featuring a lower peak value and forward shift away from the wall as compared to the smooth channel case.

Element spacing changes the point of re-attachment of the boundary layer downstream of an element; at low spacing, recirculation cells spanning the gap between adjacent elements appear. However, for given element height, spacing has a relatively weak effect on friction factor and mean velocity profile, which is somewhat surprising, given the previous results for channels with two-dimensional ribs reported in the literature. Finally, a random distribution pattern of the elements does not affect either the friction factor or the mean velocity appreciably.

The findings of this study are potentially relevant to subcooled boiling heat transfer applications where hemispherical bubbles may be attached to the heated wall in the region downstream of the bubble nucleation onset. Such bubbles effectively act as roughness elements, therefore using the laws of smooth wall channel flow would give an under-prediction of the friction factor in this case. An extension of the present study would be to investigate the effect of actual hemispherical bubbles attached to the walls, which would entail use of an interface tracking method (e.g. volume of fluid), and application a slip boundary condition at the bubble/flow interface.

Acknowledgements

This work was supported by the U.S. Department of Energy (DOE) through the Consortium for Advanced Simulation of Light Water Reactors (CASL) project.

Appendix A. Appendix-quality and grid convergence of LES

The quality of the LES simulations can be judged based on the comparison with the DNS results which are considered to be an exact solution of the Navier–Stokes equations. A quality index is introduced in Celik et al. (2005) which is based on the total turbulent kinetic energy from the DNS, k^{DNS}, and the resolved turbulent kinetic energy from the LES, k^{res}. The local turbulent kinetic energy in both cases has been computed as:

$$k = \frac{1}{2}\sqrt{\overline{(u')^2} + \overline{(v')^2} + \overline{(v')^2}} \quad \text{(A-1)}$$

Table 7
Quality index for the LES simulations.

LES for $Re_\tau = 400$	Grid 1	Grid 2	Grid 3
IQ_LES_{smooth}	0.941	0.957	0.967
$IQ\_LES_{hemisphere}$	0.99	0.995	0.997

Table 8
Convergence for LES and DNS cases.

LES smooth		DNS smooth		LES hemispherical	
$R\,(U^+_{cent})$	$R\,(k)$	$R\,(U^+_{cent})$	$R\,(k)$	$R\,(U^+_{cent})$	$R\,(k)$
0.42	0.35	0.82	0.54	0.76	0.84

where the bar sign above the velocity fluctuations indicates time average. The overall turbulent kinetic energy has been computed as the integral of Eq. (A-1) over the entire computational domain. The quality index is then given by the following equation

$$IQ\_LES = 1 - \frac{|k^{DNS} - k^{res}|}{k^{DNS}} \tag{A-2}$$

The closer the index is to unity, the higher the "quality" of the LES simulations is, as it is able to capture more of the turbulent kinetic energy. The values of IQ_LES for our simulations are shown in Table 7. Note that the quality of all these LES simulations is high, as the resolved turbulent kinetic energy is >94% of the kinetic energy computed in the DNS simulation. By comparison, the quality index in the simulations has values of the order of 95%.

Obviously, the index in Eq. (A-2) cannot be the only measure by which the quality of a LES simulation is judged. Detailed comparison of the velocity and turbulent stress distributions to their DNS counterparts also has to be made, as shown in the main body of the paper.

The solution verification methodology recommended by Rider et al. (2010) was applied to both the LES and DNS simulations. Three solutions g^k were obtained for different grid resolutions, for $k = vc, c, f$, where k is defined as 'very coarse ($k = vc$)', 'coarse ($k = c$)' and 'fine ($k = f$)', as shown in Tables 2 and 3 of the main body of the paper. The ratio of the signed error in the solution from one mesh refinement to the next can be used as a means to characterize the solution convergence:

$$\begin{aligned} &R = (g^f - g^c)/(g^c - g^{vc}) \\ &\textit{if } R < 1 \textit{ then monotonic convergence} \\ &\textit{else if } R > 1 \textit{ then monotonic divergence} \\ &\textit{else if } R < -1 \textit{ then oscillatory divergence} \\ &\textit{else } (-1 < R < 0) \textit{ then oscillatory convergence} \end{aligned} \tag{A-3}$$

For the solution verification analysis, one integral and one field variable were chosen as figures of merit: (i) the space- (x and z directions) and time-averaged centerline ($y = h$) streamwise velocity, and (ii) the turbulent kinetic energy of the entire domain (integral quantity). The results are shown in Table 8. The solution exhibits monotonic convergence for all figures of merit.

References

Ashrafian, A., Andersson, H.I., Manhart, M., 2004. Dns of turbulent flow in a rod-roughened channel. Int. J. Heat Fluid Flow 25 (3), 373–383.

Bailon-Cuba, J., Leonardi, S., Castillo, L., 2009. Turbulent channel flow with 2d wedges of random height on one wall. Int. J. Heat Fluid Flow 3 (5).

Beckermann, C. et al., 1999. Modelling melt convection in phase-field simulations of solidification. J. Comp. Phys. 154, 468–496.

Bhaganagar, K., Kim, J., Coleman, G., 2004. Effect of roughness on wall-bounded turbulence. Flow, Turbulence Combust. 72 (2–4), 463–492.

Celik, I.B., Cehreli, Z.N., Yavuz, I., 2005. Index of resolution quality for large eddy simulations. J. Fluids Eng. 127, 949–958.

Coceal, O. et al., 2006. Mean flow and turbulence statistics over groups of urban-like cubical obstacles. Boundary-Layer Meteorol 121, 491–519.

Colebrook, C.F., 1939. Turbulent flow in pipes, with particular reference to the transition region between smooth and rough pipe laws. J. Inst. Civil Eng. (London) 11 (4), 133–156.

Groetzbach, G., 1983. Spatial resolution requirements for direct numerical simulation of the Rayleigh-Benard convection. J. Comp. Phys. 49, 241–264.

Hanjalic, K., Launder, B., 1972. Fully developed asymmetric flow in a plane channel. J. Fluid Mech. 51, 301–335.

Hoyas, S., Jimenez, J., 2008. Reynolds number effects on the reynolds-stress budgets in turbulent channels. Phys. Fluids 20, 101511.

Ikeda, T., Durbin, P.A., 2007. Direct simulation of a rough-wall channel flow. J. Fluid Mech. 571, 235–263.

Jimenez, J., 2004. Turbulent flows over rough walls. Annu. Rev. Fluid Mech. 36, 173–196.

Krogstad, P.-Å., Antonia, R.A., Browne, L.W.B., 1992. Comparison between rough- and smooth-wall turbulent boundary layers. J. Fluid Mech. 245, 599–617.

Krogstad, P.-Å. et al., 2005. An experimental and numerical study of channel flow with rough walls. J. Fluid Mech. 530, 327–352.

Labois, M., Narayanan, C., Lakehal, D. 2010. On the prediction of boron dilution with the cmfd code transat: the rocom test case. In: Proc. CFD4NRS 4. OECD-NEA, 14–16 November, Washington, USA.

Leonardi, S., Castro, I.P., 2010. Channel flow over large cube roughness: a direct numerical simulation study. J. Fluid Mechan. 651, 519–539.

Leonardi, S. et al., 2003. Direct numerical simulations of turbulent channel flow with transverse square bars on one wal. J. Fluid Mech. 491, 229–238.

Leonardi, S., Orlandi, P., Antonia, R.A., 2007. Properties of D- and K-type roughness in a turbulent channel flow. Phys. Fluids 19, 125101.

Mittal, R., Iaccarino, G., 2005. Immersed boundary methods. Ann. Rev. Fluid Mech. 37 (1), 239–261.

Miyake, Y., Tsujimoto, K., Masaru, N., 2001. Direct numerical simulation of rough wall heat transfer in a turbulent channel flow. Int. J. Heat Fluid Flow 22, 237–244.

Nagano, Y., Hattori, H., Houra, T., 2004. Dns of velocity and thermal fields in turbulent channel flow with transverse rib roughness. Int. J. Heat Fluid Flow 25, 393–403.

Nicoud, F., Ducros, F., 1999. Subgrid-scale stress modelling based on the square of the velocity gradient tensor. Flow, Turbulence Combust. 62, 183–200.

Nikuradse, J., 1950. Laws of Flow in Rough Pipes. VDI Forschungsheft 361, 1933. NACA TM 1292.

Orlandi, P., Leonardi, S., Antonia, R.A., 2006. Turbulent channel flow with either transverse or longitudinal roughness elements on one wall. J. Fluid Mech. 561, 279–305.

Perry, A.E., Schofield, W.H., Joubert, P.N., 1969. Rough wall turbulent boundary layers. J. Fluid Mech. 37, 383–413.

Peskin, C.S., 1977. Numerical analysis of blood flow in the heart. J. Comp. Phys. 25, 220–234.

Rider, W.J., Kamm, J.R., Weirs, V.G. 2010. Code Verification Workflow in CASL, Report SAND2010-7060P, Sandia National Laboratories, September.

Smagorinsky, J., 1963. General circulation experiments with the primitive equations. I. The basic experiment. Month. Wea. Rev. 91, 99–164.

Townsend, A.A., 1976. The Structure of Turbulent Shear Flow. C.U. Press, Cambridge, UK.

Van Driest, E.R., 1956. On turbulent flow near a wall. J. Aero. Sci. 23, 1007–1011.